

# LED-based hyperspectral endoscopic imaging: Optical simulation-guided illumination optimization

Tianao Li <sup>a,b</sup>, Naeeme Modir <sup>a,b</sup>, Baowei Fei <sup>a,b,c,\*</sup>

<sup>a</sup> Department of Bioengineering, University of Texas at Dallas, Richardson, Texas

<sup>b</sup> Center for Imaging and Surgical Innovation, University of Texas at Dallas, Richardson, Texas

<sup>c</sup> Department of Radiology, University of Texas Southwestern Medical Center, Dallas, Texas

\* Corresponding author: [bfei@utdallas.edu](mailto:bfei@utdallas.edu), Website: <https://fei-lab.org>

## ABSTRACT

Digestive system cancers, particularly esophageal cancer, remain difficult to detect in early stages due to the limited sensitivity of conventional white-light endoscopy. Hyperspectral endoscopic imaging enhances tissue contrast by exploiting wavelength-dependent optical properties. However, its performance depends on efficient and uniform spectral illumination under highly constrained and asymmetric endoscope tip geometries. In practice, the imaging sensor is offset from the center due to the existence of instrument channels and air/water nozzles, complicating LED placement and degrading illumination uniformity. In this work, we present an optical simulation-driven framework for optimizing LED placement in an LED-based, asymmetric hyperspectral endoscopic illumination system. Non-sequential ray tracing and merit-function-based optimization were implemented in Zemax OpticStudio to optimize LED spatial configurations. Two local optimization algorithms—Damped Least Squares (DLS) and Orthogonal Descent (OD)—were systematically evaluated across fifteen wavelength groups. Both methods achieved measurable improvements in irradiance distribution. Overall, OD slightly outperformed DLS, yielding average irradiance improvements of 11.30% on the esophagus wall and 10.15% on the LED field of view relative to the pre-optimization configuration, whereas DLS achieved corresponding average increases of 7.03% and 6.55%, respectively. Rather than prescribing a fixed LED placement pattern, the results provide practical design guidance by demonstrating how adaptive, optimization-driven LED positioning can effectively compensate for asymmetric endoscope geometries while prioritizing different illumination targets. These findings demonstrate that simulation-based LED placement optimization can provide effective guidance for the design of hyperspectral endoscopic illumination systems, high-fidelity modeling, and experimental validation.

**Keywords:** Hyperspectral imaging, optical simulation, endoscopy, LED, image-guided endoscopic procedure

## 1. INTRODUCTION

Digestive cancers continue to impose a significant health burden. In the United States alone, more than 360,000 new cases and approximately 175,000 deaths from digestive system cancers are expected in 2025 [1]. Esophageal cancer remains particularly challenging, as its precursor condition, Barrett's esophagus, affects approximately 1.6–6.8% of the general population, and early dysplastic changes are difficult to detect using conventional endoscopy [2]. These statistics point out the need for improved endoscopic imaging techniques capable of enhancing early lesion detection.

Conventional white-light endoscopy remains the clinical standard for gastrointestinal cancer screening; however, its diagnostic sensitivity is limited for subtle or early-stage lesions. Recent clinical and technical reviews emphasize that improvements in image quality, contrast mechanisms, and diagnostic reliability are critical for advancing gastrointestinal endoscopy and reducing operator dependence [3, 4]. Consequently, optical imaging approaches that extend beyond intensity-based visualization have attracted increasing interest.

Advanced optical contrast mechanisms, such as polarimetric imaging, have demonstrated sensitivity to tissue microstructural alterations associated with pathological progression, revealing diagnostic information not readily visible under white-light illumination [5]. Among these approaches, hyperspectral imaging (HSI) has emerged as a powerful modality by capturing spatially resolved spectral information that reflects tissue biochemical and vascular characteristics. Foundational work has established the principles and biomedical potential of HSI while highlighting key challenges related to acquisition speed and system complexity [6].

Recent developments in hyperspectral endoscopy have focused on achieving real-time performance suitable for clinical use. While snapshot hyperspectral techniques enable simultaneous acquisition of spatial, spectral, and temporal information [7], wavelength-switching hyperspectral imaging remains widely adopted due to its high spatial resolution, higher spectral flexibility, and compatibility with LED-based illumination [8].

In parallel, LED-based spectral illumination has gained prominence as a practical solution for compact and flexible hyperspectral imaging systems. Optimized LED-driven architectures have demonstrated precise wavelength control, efficient temporal modulation, and reduced system complexity, enabling real-time spectral imaging in endoscopic settings [9, 10]. However, these existing designs primarily assume a centrally located imaging sensor and radially symmetric illumination geometry, which simplifies LED placement and optical optimization. In practical endoscopic systems, the imaging sensor is typically offset from the optical axis, and the limited space at the endoscope tip imposes asymmetric constraints on LED placement and printed circuit board (PCB) design, leading to nonuniform illumination and degraded irradiance distribution. Such nonuniform illumination can introduce spatially varying intensity and spectral bias across the field of view, which obscures subtle tissue contrast, complicates quantitative spectral interpretation, and reduces the reliability of abnormality detection in endoscopic imaging [11].

To address these challenges, the present work focuses on optical simulation-driven design and optimization of LED placement under asymmetric geometric constraints. By using the non-sequential ray tracing and merit-function optimization in Zemax, this study optimized LED spatial configurations to improve irradiance while maintaining illumination uniformity on the target surface. This approach enables realistic modeling of endoscope tip geometry and provides a quantitative framework for optimizing LED-based hyperspectral illumination beyond idealized, centrally symmetric configurations. Furthermore, such physically optimized illumination is essential for downstream spectral analysis and multimodal data processing, which have been shown to enhance diagnostic sensitivity for esophageal cancer detection [11].

## 2. METHOD

The LED Array, serves as the illuminance module of our proposed imaging system, is simulated in Ansys Zemax OpticStudio (2025 R1.00) with non-sequential mode (NSC mode). Specifically, we mirrored the radiant power and wavelength for each LED group. LED locations are set as variables for optimization. Boundary conditions and constraints are defined for coordinates initialization and optimization. Power detectors are placed in the regions of interest (ROI) for illuminance condition evaluation and sequential optimization. Figure 1 shows the schematic of the LED array PCB and the detailed diagram of the workflow including presetting, model configuration, optimization, post-processing and evaluation. The simulation was implemented on an Intel Xeon Silver 4215R CPU with 8 cores and 16 threads.

### 2.1 Simulation Model Configuration

To mimic the actual clinical condition of endoscopy, in which the endoscope is inserted and navigated through the esophagus for imaging acquisition, an annular volume object was used as a simplified approximation of the tubular geometry of the esophagus. The inner and outer radius of the esophagus segment were defined as 5 mm and 5.5 mm, respectively, consistent with reported adult esophageal lumen diameters of approximately 10–12 mm under minimally distended conditions and typical esophageal wall thicknesses of 0.5–1 mm [12-14]. The length of the segment was set as 19 mm because the analysis mainly focuses on the endoscope tip. A 3D model of the LED Array PCB was created via AutoCAD Fusion 360 and further imported into Zemax for visualization of the location of the LED Array plane. A total of 60 source points were used to model the LEDs with the wavelengths and power values matched to the datasheet. All the LEDs used are bare chip micro-LEDs with viewing angle of 120 degrees. Detectors were placed to measure the irradiance and illumination uniformity at the regions of interest (ROIs). The colon segment object itself was defined as the detector, which allows us to extract the signal from the inner surface. Another ROI is the field of view (FOV) of the LED array and the camera. For the LED array, a 12 mm by 12 mm detector rectangle was placed 5 mm away from the LED plane. Similarly, a smaller (3 mm by 3 mm) detector rectangle was defined as camera FOV at the same working distance. The resolution was set as 100 pixels by 100 pixels for both detectors.

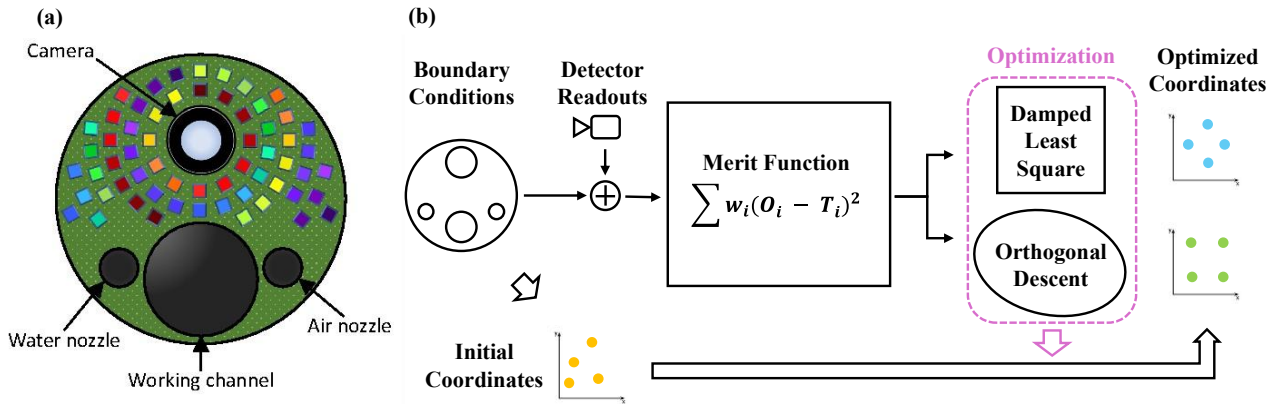


Figure 1. (a) The schematic of LED array PCB. (b) The workflow of LED position optimization in a non-sequential optical simulation framework. Starting from initial coordinates, the system applies predefined boundary conditions (geometric and physical constraints) to ensure feasible LED placement, and the resulting optical response is evaluated through detector readouts that quantify performance metrics such as irradiance or uniformity. These detector outputs are fed into a merit function formulated as a weighted least-squares objective. The merit function is then minimized using numerical optimization algorithms, specifically Damped Least Squares (DLS) and Orthogonal Descent (OD). Through iterative updates, the optimizer adjusts the LED coordinates while respecting boundary constraints, and this loop continues until convergence, yielding optimized coordinates that improve the desired optical performance compared with the initial configuration.

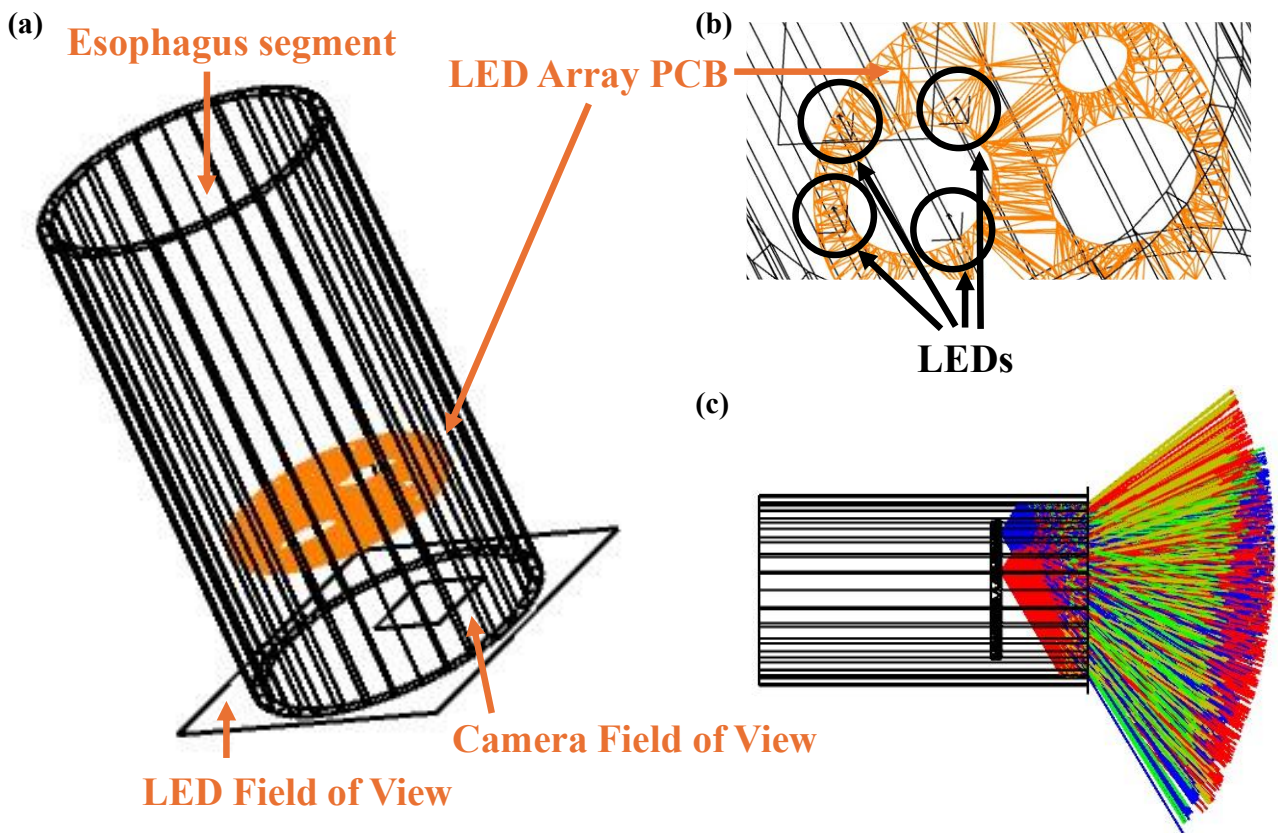


Figure 2. (a) The simulation model with each component highlighted; (b) The zoomed in LED array PCB where the first LED group was highlighted; (c) The overall layout of the model when display rays were defined, representing LEDs turned ON.

For each LED, a total number of  $1 \times 10^6$  were traced for quantitative computation. Such high calculation ray count was selected to reduce Monte Carlo noise and ensure stable detector readouts [15]. However, to release the computation burden, a smaller count of display ray (1000 per LED) was selected only for visualization purposes. Figure 2 shows the model configuration.

## 2.2 Coordinates Initialization

Initially, LEDs were distributed on the PCB under predefined geometric constraints. As illustrated in Figure 3a, a typical endoscope tip contains multiple functional apertures, including openings for surgical instruments, the imaging camera, and water and air nozzles. To simplify the simulation while preserving physical realism, the allowable LED placement area was defined as the upper semicircular region of the PCB, excluding the camera aperture (Figure 3c).

Table 1. The distribution of wavelength groups for compartmentalization regions.

Region	1	2	3	4	5	6 & 7	Total
Num of Wavelength Groups	1	1	2	3	4	4	15
Wavelength (nm)	980	950	890/910	800/830/850	630/670/700/740	395/430/505/525	

Previous studies have demonstrated that shorter wavelengths experience stronger scattering and absorption in biological tissues compared with longer wavelengths due to Rayleigh and Mie scattering mechanisms as well as wavelength-dependent absorption characteristics [16-18]. In addition, most optical imaging sensors exhibit higher quantum efficiency (QE) at longer wavelengths, resulting in more efficient photon detection in the red and near-infrared spectral range [19-21]. Consequently, illumination at shorter wavelengths suffers from a dual disadvantage: increased optical loss during tissue propagation and reduced detection efficiency at the sensor.

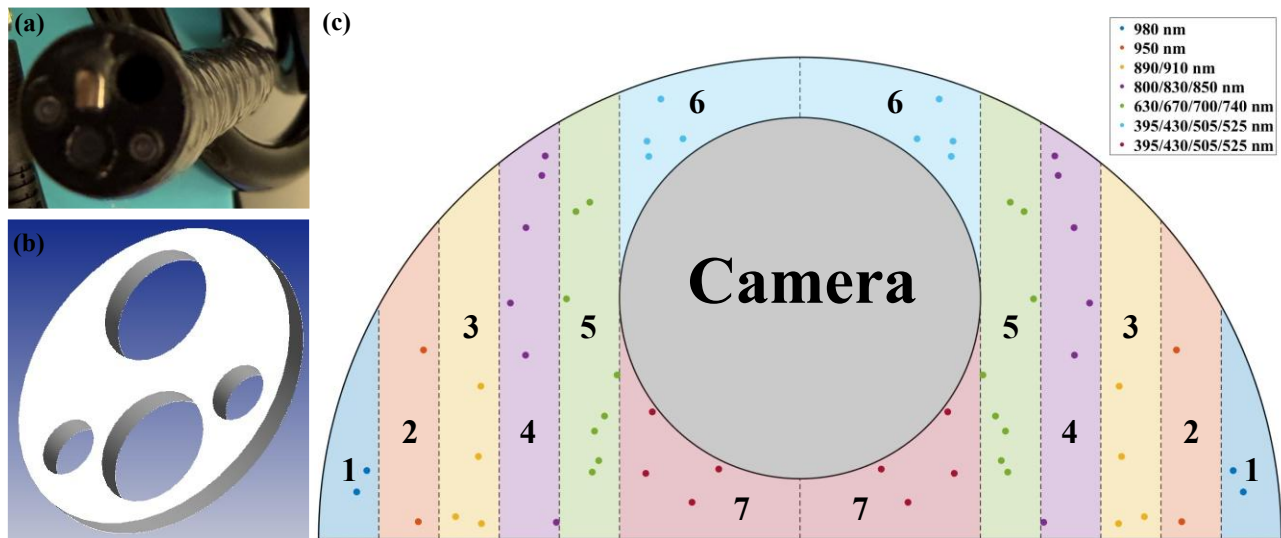


Figure 3. (a) The photo of a commercial endoscope tip; (b) The 3D model of the LED array PCB to approximate the holes on the endoscope tip in (a); (c) The compartmentalization of the LED allowable area with different colors and region number labels. The dots in each region showed the positions for all 60 LEDs.

To compensate for these effects and achieve comparable irradiance levels at the imaging plane, shorter-wavelength LEDs must be positioned closer to the camera, thereby reducing the optical path length and minimizing scattering- and absorption-induced attenuation. This placement strategy ensures sufficient photon flux reaches the detector and helps balance the effective contribution of each wavelength band in the final image.

Based on this principle, the allowable region was first compartmentalized into seven sub-regions, and all fifteen wavelength groups were assigned accordingly, as summarized in Table 1. Within each region containing multiple wavelength groups, the generated LED coordinates were ranked by their distance from the camera center, and positions closer to the camera were assigned to shorter-wavelength groups. In an ideal symmetric endoscope configuration with a centrally positioned camera, illumination uniformity can be readily achieved by distributing LEDs evenly around the camera. However, the asymmetric camera position in the present design introduces additional challenges for achieving high uniformity. To address this, an axially symmetric placement strategy was adopted: LED regions were mirrored with respect to the camera's vertical symmetry axis, and LEDs belonging to the same wavelength group were constrained to share identical y-coordinates. This design maintains balanced angular illumination while accommodating the asymmetric geometry of the endoscope tip. Here, regions 6 and 7 contain the same wavelength group because they are geometrically symmetric with respect to the camera center. By assigning identical LED groups to these regions and initializing their positions using left-to-right mirroring, the four individual LEDs within the same group are evenly distributed around the camera. Such symmetric distribution significantly reduces illuminance heterogeneity across the imaging area.

LED coordinates were set as variables, which allows adjustments for optimal outcome achievement. Same conditions were applied for optimization. Axial symmetric distribution pattern of LEDs was maintained by correlating the coordinates of LED in right region to left region. Specifically, the x and y coordinates of LED in left region were defined as flexible variables which can be manipulated in optimization process. The coordinates of LED in right region, however, were defined as pickup, which picks those flexible LED as master and uses the customized settings to calculate the coordinates. Here we customized the pickup settings to ensure an axial symmetric layout:

$$\begin{cases} x_r = 2 * x_0 - x_l \\ y_r = y_l \end{cases}$$

Where  $(x_l, y_l)$ ,  $(x_r, y_r)$  represents the coordinates of left and right LED, respectively.  $x_0$  means the x coordinates of PCB/camera center. Restricting LEDs inside the PCB circular boundary and particular region were achieved through operands which are part of the merit function (MF) definition in Section 2.3.

### 2.3 Merit Function Definition

The merit function was constructed to enforce geometric conditions and quantitatively evaluate illuminance performance resulting from different LED placements during the optimization process. In general, the merit function is defined as:

$$MF = \sum w_i(O_i - T_i)^2$$

Where  $w_i$  means the weight of the  $i$ -th operand,  $O_i$  and  $T_i$  represent the value and target of the  $i$ -th operand, respectively. The merit function value (MFV) is the sum of all weighted squared deviations. The relative ratio of each operand term to the total MFV defines its contribution (%), which indicates the importance of that operand during optimization. As mentioned in Section 2.2, constraint operands were added to restrict the LED in allowable area. These operands act as penalty functions and impose an extremely high contribution (approximately 100%) when the corresponding constraints are violated. Consequently, geometric feasibility is strictly enforced throughout the optimization process.

For example, NPXL operand stands for non-sequential object x position should be less than a specific coordinate (set as target value in Merit Function Editor). If the actual object shifted out of this boundary, the contribution of this operand will be forced to 99.75%, which dominates the overall function and lifts the MFV. The optimization will adjust the variables (LED coordinates) to reduce the MFV by placing the LED in the boundary. Once the violation is cleared, the contribution will be set as 0 which won't influence the operands for actual optimization.

To quantify illumination performance, detector readout operands were inserted for the three detectors to acquire the quantitative measurements. These detectors monitor the average irradiance on the esophagus inner wall, the LED field-of-view (FOV) plane, and the camera FOV plane, respectively. Illuminance uniformity was evaluated by returning the standard deviation of irradiance over the camera FOV detector. The result shows an average value of  $1.9 \times 10^{-7}$  which is substantially lower than the baseline value (mean value of  $2.1 \times 10^{-2}$ ), suggesting highly homogenous illumination owing to the axial symmetric pattern. This result is further supported by the detector viewer heatmap of camera FOV detector, as shown in Figure 4b.

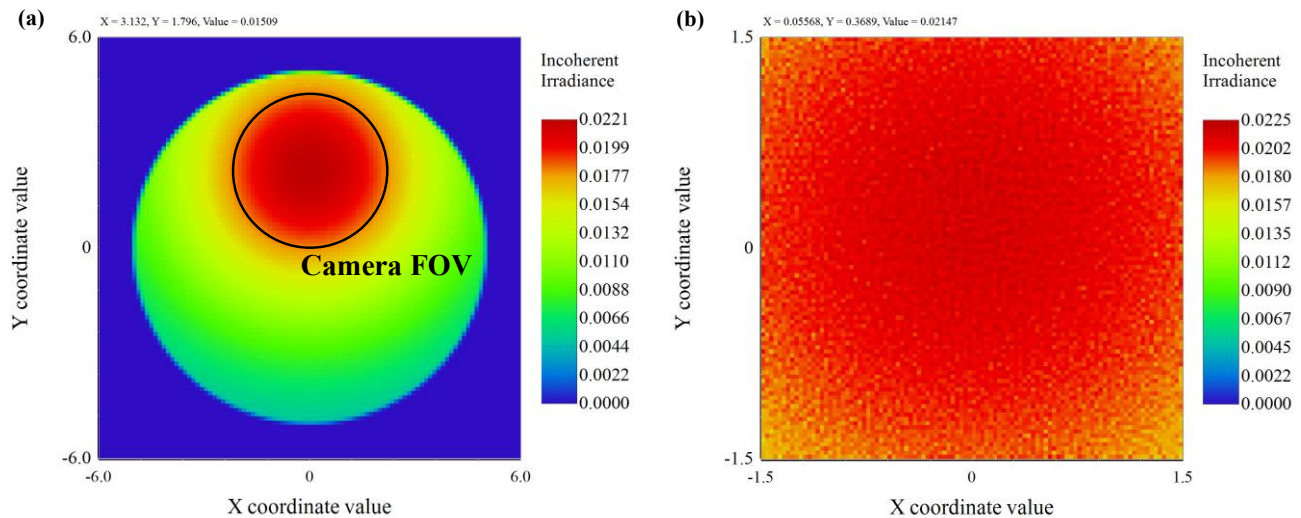


Figure 4. Irradiance readout in detector viewer when the four 395 nm LEDs were activated. (a) Irradiance distribution over the LED field of view (12 mm by 12 mm). Regions outside the circular boundary corresponding to the esophagus cylinder show no irradiance due to blockage, while the camera field of view exhibits the highest irradiance with a peak irradiance of  $0.0221 \text{ W/cm}^2$ ; (b) Enlarged view of the camera field of view (3 mm by 3 mm), showing a peak irradiance of  $0.0225 \text{ W/cm}^2$ . The slight difference in peak values between (a) and (b) arises from detector resolution effects, as both detectors use the same number of pixels and report mean irradiance per pixel, leading to averaging in the larger LED field of view.

The optimization strategy aimed to balance irradiance levels on the esophagus wall and LED FOV while simultaneously increasing the illumination intensity at the camera FOV. Accordingly, convergence toward the average irradiance value was set as the optimization target for the esophagus and LED FOV detectors, whereas the target for the camera FOV detector was defined as a 50% increase relative to the baseline configuration. Operand weights were carefully tuned to balance the relative influence of each detector metric within the overall merit function.

As the detector-based evaluation relies on Monte Carlo ray tracing, the merit function exhibits inherent noise, which influenced the choice and behavior of optimization algorithms discussed in Section 2.4.

## 2.4 Optimization

Two optimization algorithms available in Zemax OpticStudio, Damped Least Squares (DLS) and Orthogonal Descent (OD), were applied independently to optimize the LED placement. Identical model parameters, initial conditions, constraints and merit function definition were applied for these two methods. The optimization was performed in an iterative manner, with the optimizer running continuously until convergence behavior was observed. MFV was monitored visually through the optimization progress window, and the optimization process was terminated manually when the MFV reached a stable plateau and no further noticeable reduction was observed over successive iterations. During optimization, operand contributions were inspected to verify that constraint operands were inactive once geometric feasibility was achieved and that detector-based operands dominated the final stage of the optimization.

## 2.5 Optimization Results Evaluation

The optimization results were evaluated from two perspectives: basic optimization information describing the convergence behavior of each optimization run, and illumination performance improvement quantified by detector-based irradiance metrics.

For each LED wavelength group, Damped Least Squares (DLS) and Orthogonal Descent (OD) optimizations were performed independently under identical merit function definitions and geometric constraints. The optimization process was characterized by the total number of optimization cycles executed, the overall simulation time, and the net change in MFV between the initial configuration and the final converged state. The number of cycles represents the total cycles

executed until convergence was observed, and the simulation time was measured from the start of optimization to manual termination once the MFV reached a stable plateau.

Illumination performance improvement was evaluated using the irradiance readouts change. For each optimization run, detector readouts were recorded before optimization and after convergence. The relative change in average irradiance for each detector was calculated as

$$\Delta I(\%) = \frac{I_{opt} - I_{init}}{I_{init}} \times 100$$

Where  $I_{init}$  and  $I_{opt}$  are the average irradiance before and after optimization, respectively.

### 3. RESULTS

#### 3.1 Optimization Basics

Tables 2 and 3 summarize the cycle numbers, optimization time, and MFV reduction percentages for each wavelength group obtained using the two optimization algorithms. Although the cycle definitions differ between the two methods, their overall optimization performance in terms of MFV reduction was largely consistent across most wavelengths. Both algorithms achieved comparable MFV decreases within similar total optimization times.

In the OD approach, the cycle count was divided into sub-cycles, with each major cycle requiring approximately 10 minutes, whereas in DLS each cycle took about 1 minute. A pronounced MFV reduction of approximately 10% was observed after the first major OD cycle (denoted as cycle 2-1, corresponding to the start of the second cycle). Overall, OD achieved a higher average MFV reduction (10.81%) with slightly shorter total optimization time (12.3 min) compared to DLS (8.22% MFV reduction in 14.8 min). This was further supported by Figure 5a. Nevertheless, for certain wavelength groups, DLS produced comparable MFV reductions with substantially shorter optimization times.

Table 2. Optimization cycle, time and merit function value change for all wavelength groups by DLS algorithm.

Wavelength (nm)	395	430	505	525	630
Cycle	13	12	11	24	10
Time (min)	12.16	11.75	13.44	23.17	13.14
MFV change	4.31%	5.32%	7.97%	8.50%	6.43%
Wavelength (nm)	670	700	740	800	830
Cycle	12	19	11	16	16
Time (min)	16.32	22.51	11.76	18.08	17.98
MFV change	4.03%	7.33%	15.62%	7.58%	7.19%
Wavelength (nm)	850	890	910	950	980
Cycle	10	7	7	20	11
Time (min)	12.01	8.14	10.18	26.18	4.67
MFV change	0.65%	10.30%	21.40%	5.43%	11.43%

Table 3. Optimization cycle, time and merit function value change for all wavelength groups by OD algorithm.

Wavelength (nm)	395	430	505	525	630
Cycle	2-1	2-4	2-2	2-1	2-1
Time (min)	8.06	13.54	11.12	11.33	11.18
MFV change	6.09%	6.86%	10.14%	9.14%	10.51%
Wavelength (nm)	670	700	740	800	830
Cycle	2-1	2-1	2-1	2-4	2-3
Time (min)	9.12	10.66	11.54	18.11	13.47
MFV change	5.17%	9.38%	15.81%	8.68%	8.32%
Wavelength (nm)	850	890	910	950	980
Cycle	2-1	2-2	2-1	2-4	4-1
Time (min)	10.85	12.44	10.15	20.27	12.67
MFV change	11.30%	14.44%	21.69%	9.47%	15.07%

### 3.2 Illuminance Performance Improvement

Following optimization, irradiance readout changes were calculated for both methods using the formulation described in Section 2.5. The resulting change ratios were compared and are presented in Figure 5b–5d. On average, the irradiance within the esophagus ROI and the LED FOV was balanced to an approximate 10% change ratio using the OD method, indicating effective optimization. In comparison, DLS produced average change ratios of 7.03% and 6.55% for the same ROIs, respectively, which were consistent with its overall MFV reduction.

For the camera FOV, a clear irradiance increase was observed across most wavelengths when using DLS. In contrast, the OD method exhibited unexpected irradiance decreases at certain wavelengths. This behavior is likely attributable to the different MFV reduction strategy employed by OD, in which optimization favored the esophagus and LED FOV regions at the expense of the camera FOV. Consequently, sacrificing camera FOV irradiance contributed to a larger overall reduction in the merit function value, which also explains the relatively low average change ratio of 2.27% observed in this region. Nevertheless, when examined at individual wavelengths, substantial improvements, reaching change ratios of up to 20%, were achieved for specific wavelength groups.

Negligible optimization improvement was observed for certain wavelength groups even after sufficient optimization time and multiple cycles. One plausible explanation is that the initial LED configurations for these wavelengths were already positioned near a local minimum of the merit function, leaving limited room for further improvement. In such cases, the optimizer primarily performed fine-scale parameter adjustments that resulted in only marginal changes to the MFV. Additionally, the constrained geometric layout of the endoscope tip and the strong coupling between LED position and irradiance distribution may further restrict the feasible solution space, reducing the optimizer’s ability to achieve significant performance gains for these wavelengths.

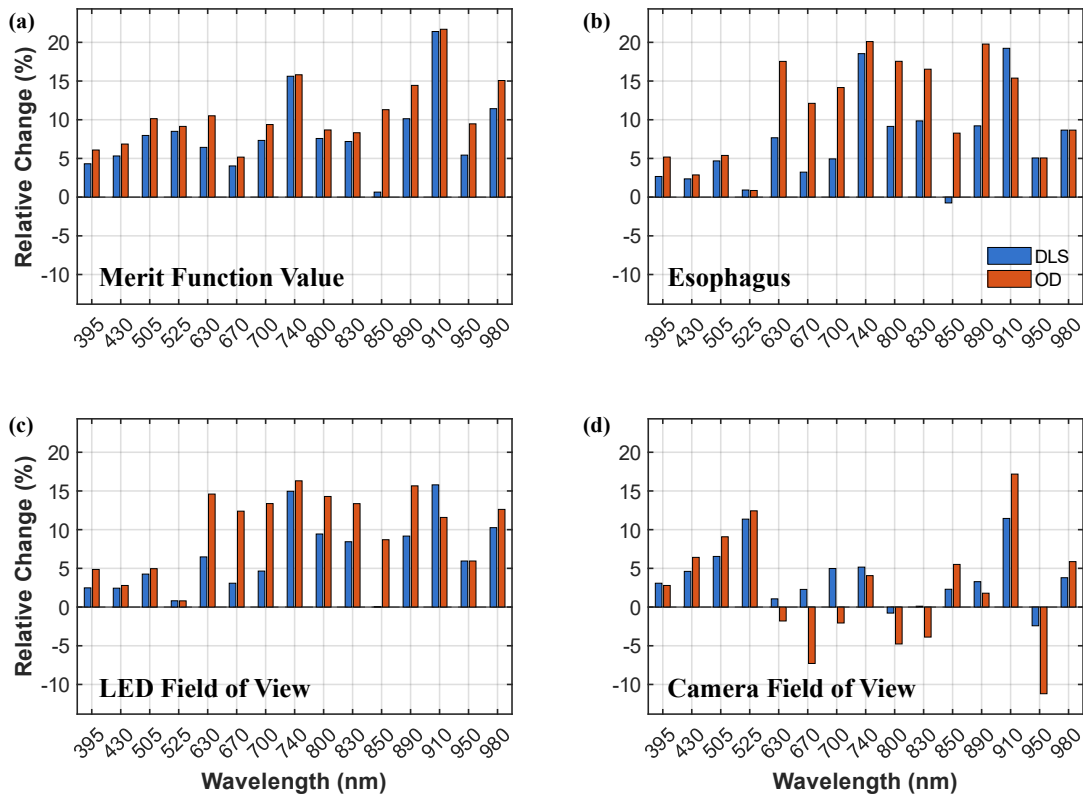


Figure 5. Comparison of optimization performance between the Damped Least Squares (DLS) and Orthogonal Descent (OD) algorithms across all wavelength groups. (a) Relative change in merit function value (MFV) after optimization; (b) Relative change in the average irradiance measured on the esophagus wall detector; (c) Relative change in the average irradiance over the LED field-of-view (FOV) detector; (d) Relative change in the average irradiance within the camera FOV.

## 4. DISCUSSION AND CONCLUSION

This work demonstrates that systematic optical optimization can effectively improve illumination performance in constrained endoscopic geometry. Meaningful reductions in the merit function value were achieved across most wavelength groups, accompanied by balanced irradiance redistribution between the esophagus and LED fields of view, as well as improved irradiance on the camera field of view. The illuminance uniformity was also maintained by an axial symmetric pattern. These results validate the feasibility of using optical simulation-based optimization to guide LED placement design for multispectral endoscopic imaging systems.

To reduce computational complexity and ensure stable convergence, the optical model incorporated several simplifying assumptions in geometry and boundary conditions. The allowable LED placement region was restricted to the upper semicircular area, thereby avoiding the lower half of the endoscope tip, where the presence of water and air nozzles would significantly complicate boundary definition and optical interactions. In addition, LEDs were modeled as idealized point sources, neglecting the finite physical dimensions and emission area of the LED chips. Spatial constraints on the minimum separation between LEDs, both within and across compartmentalized sub-regions, were also not considered in the current model.

These simplifications were intentionally introduced to isolate the dominant factors governing illumination uniformity and irradiance distribution while keeping the optimization problem tractable for systematic comparison between OD and DLS methods. Although fine-scale geometric effects and manufacturing constraints were not explicitly modeled, the simplified configuration preserves the relative spatial relationships between LEDs and regions of interest, which primarily determine the irradiance balance in the endoscopic field. Consequently, the optimization results remain physically meaningful and provide valuable design guidance.

The optimization in this work was performed using OD and DLS, both of which are local optimization methods. OD reduces the merit function by sequentially optimizing along orthogonal parameter directions, making it less sensitive to parameter coupling but potentially more time-consuming per cycle. In contrast, DLS uses a Jacobian-based update scheme to simultaneously adjust multiple variables, enabling faster convergence when the initial configuration is close to an optimal solution. While both methods proved effective, their local nature limits the ability to escape the local minimum. This limitation is evident in wavelength groups that exhibited negligible improvement despite extended optimization time, suggesting that the initial LED placement was already near a local optimum. Incorporating a global optimization strategy or a hybrid approach that combines global exploration with OD or DLS refinement may further enhance robustness and overall performance in future studies.

## ACKNOWLEDGEMENT

Research reported in this publication was supported in part by the National Cancer Institute of the National Institutes of Health under Award Number R01CA288379, the Cancer Prevention and Research Institute of Texas (CPRIT) under Award Number RP240289 and RP240542, and the Eugene McDermott Graduate Fellowship (EMGF) 202506 at the University of Texas at Dallas. The content is solely the responsibility of the authors and does not necessarily represent the official views of the National Institutes of Health.

## REFERENCES

- [1] R. L. Siegel, T. B. Kratzer, A. N. Giaquinto *et al.*, “Cancer statistics, 2025,” *CA: A Cancer Journal for Clinicians*, 75(1), 10-45 (2025).
- [2] P. J. F. de Jonge, M. van Blankenstein, W. M. Grady *et al.*, “Barrett's oesophagus: epidemiology, cancer risk and implications for management,” *Gut*, 63(1), 191-202 (2014).
- [3] C. Ferrari, and M. Tadros, “Enhancing the Quality of Upper Gastrointestinal Endoscopy: Current Indicators and Future Trends,” *Gastroenterology Insights*, 15(1), 1-18 (2024).
- [4] Y. Tang, S. Anandasabapathy, and R. Richards-Kortum, “Advances in optical gastrointestinal endoscopy: a technical review,” *Molecular Oncology*, 15(10), 2580-2599 (2021).
- [5] A. Pierangelo, A. Nazac, A. Benali *et al.*, “Polarimetric imaging of uterine cervix: a case study,” *Optics Express*, 21(12), 14120-14130 (2013).

- [6] G. Lu, and B. Fei, "Medical hyperspectral imaging: a review," *Journal of biomedical optics*, 19(1), 010901-010901 (2014).
- [7] H.T. Lim, and V. M. Murukeshan, "A four-dimensional snapshot hyperspectral video-endoscope for bio-imaging applications," *Scientific Reports*, 6(1), 24044 (2016).
- [8] C. M. Browning, R. Cloutier, T. C. Rich *et al.*, "Endoscopy Lifetime Systems Architecture: Scoping Out the Past to Diagnose the Future Technology," *Systems*, 10(5), 189 (2022).
- [9] N. Modir, M. Shahedi, J. Dormer *et al.*, "LED-based, real-time, hyperspectral imaging device," *Journal of Medical Imaging*, 12(3), 035002 (2025).
- [10] K. Pruitt, N. Modir, N. Nawawithan *et al.*, "Optimization of a real-time LED based spectral imaging system," *Proc. of SPIE BiOS*, 12853, 128530D (2024).
- [11] J. Bonaventura, N. Lima, J. Routh *et al.*, "Multimodal esophageal cancer imaging: establishing data processing techniques and assessing diagnostic sensitivity," *Biophotonics Discovery*, 2(2), 022704 (2025).
- [12] S. Standring, H. Ellis, J. Healy *et al.*, "Gray's anatomy: the anatomical basis of clinical practice," *American journal of neuroradiology*, 26(10), 2703 (2005).
- [13] E. Yazaki, and D. Sifrim, "Anatomy and physiology of the esophageal body," *Diseases of the Esophagus*, 25(4), 292-298 (2012).
- [14] F. Xia, J. Mao, J. Ding *et al.*, "Observation of normal appearance and wall thickness of esophagus on CT images," *European Journal of Radiology*, 72(3), 406-411 (2009).
- [15] L. Wang, S. L. Jacques, and L. Zheng, "MCML—Monte Carlo modeling of light transport in multi-layered tissues," *Computer Methods and Programs in Biomedicine*, 47(2), 131-146 (1995).
- [16] S. L. Jacques, "Optical properties of biological tissues: a review," *Physics in Medicine & Biology*, 58(11), R37 (2013).
- [17] C. Wf, "A review of the optical properties of biological tissues," *IEEE J Quantum Electron*, 26, 2166-2185 (1990).
- [18] R. Tao, J. Gröhl, L. Hacker *et al.*, "Tutorial on methods for estimation of optical absorption and scattering properties of tissue," *Journal of Biomedical Optics*, 29(6), 060801 (2024).
- [19] J. Janesick, "Scientific Charge-Coupled Devices, 83 SPIE Press," Bellingham, Washington, (2001).
- [20] Z. Deng, L. Chen, X. Wei *et al.*, "Evaluation of Average Quantum Efficiency of Industrial Digital Camera," *Sensors*, 25(3), 899 (2025).
- [21] T. M. Kim, J. Kim, S. Lee *et al.*, "A High-Performance 2.2 $\mu$ m 1-Layer Pixel Global Shutter CMOS Image Sensor for Near-Infrared Applications," *2024 IEEE International Electron Devices Meeting (IEDM)*, 1-4 (2024).